Monthly Notices
of the
ROYAL ASTRONOMICAL SOCIETY

MNRAS **433,** 1492–1504 (2013)
Advance Access publication 2013 June 4

doi:10.1093/mnras/stt831

The nature of massive black hole binary candidates – I. Spectral properties and evolution

Roberto Decarli,[1⋆] Massimo Dotti,[2,3] Michele Fumagalli,[4,5†] Paraskevi Tsalmantza,[6] Carmen Montuori,[7,8] Elisabeta Lusso,[1] David W. Hogg[1,9] and Jason X. Prochaska[10]

[1]*Max-Planck-Institut für Astronomie, Königstuhl 17, D-69117 Heidelberg, Germany*
[2]*Dipartimento di Fisica G. Occhialini, Università degli Studi di Milano Bicocca, Piazza della Scienza 3, I-20126 Milano, Italy*
[3]*INFN, Sezione di Milano-Bicocca, Piazza della Scienza 3, I-20126 Milano, Italy*
[4]*Carnegie Observatories, 813 Santa Barbara Street, Pasadena, CA 91101, USA*
[5]*Department of Astrophysics, Princeton University, Princeton, NJ 08544-1001, USA*
[6]*Klausenpfad 22, D-69121 Heidelberg, Germany*
[7]*Department of Physics, Technion, IL-32000 Haifa, Israel*
[8]*Department of Physics, Faculty of Natural Sciences, University of Haifa, Haifa 31905, Israel*
[9]*Center for Cosmology and Particle Physics, Department of Physics, New York University, 4 Washington Place, New York, NY 10003, USA*
[10]*Department of Astronomy and Astrophysics, University of California, 1156 High Street, Santa Cruz, CA 95064, USA*

Accepted 2013 May 8. Received 2013 April 30; in original form 2013 March 8

ABSTRACT

Theoretically, bound binaries of massive black holes are expected as the natural outcome of mergers of massive galaxies. From the observational side, however, massive black hole binaries remain elusive. Velocity shifts between narrow and broad emission lines in quasar spectra are considered a promising observational tool to search for spatially unresolved, dynamically bound binaries. In this series of papers, we investigate the nature of such candidates through analyses of their spectra, images and multiwavelength spectral energy distributions. Here we investigate the properties of the optical spectra, including the evolution of the broad line profiles, of all the sources identified in our previous study. We find a diverse phenomenology of broad and narrow line luminosities, widths, shapes, ionization conditions and time variability, which we can broadly ascribe to four classes based on the shape of the broad line profiles. (1) Objects with bell-shaped broad lines with big velocity shifts (>1000 km s^{-1}) compared to their narrow lines show a variety of broad line widths and luminosities, modest flux variations over a few years, and no significant change in the broad line peak wavelength. (2) Objects with double-peaked broad emission lines tend to show very luminous and broadened lines, and little time variability. (3) Objects with asymmetric broad emission lines show a broad range of broad line luminosities and significant variability of the line profiles. (4) The remaining sources tend to show moderate to low broad line luminosities, and can be ascribed to diverse phenomena. We discuss the implications of our findings in the context of massive black hole binary searches.

Key words: accretion, accretion discs – black hole physics – line: profiles – quasars: emission lines – quasars: general.

1 INTRODUCTION

In the framework of hierarchical models of galaxy formation, mergers play a key role in the build-up of galaxies. Massive black holes (BHs) ubiquitously populate the centres of galaxies (at least in massive galaxies; e.g. Kormendy & Richstone 1995; Decarli et al. 2007; Gallo et al. 2008). As a natural consequence, BH pairs wandering in merger remnants are expected. Dynamical friction efficiently drives the BHs towards the centre of the potential well, where they form a bound black hole binary (BHB). The subsequent evolution of these systems is poorly understood. At separations of a few parsecs, dynamical friction becomes inefficient, and the binary may stall (the so-called last parsec problem; for recent reviews, see Colpi & Dotti 2009; Dotti, Sesana & Decarli 2012). If this limit is overcome, and the binary reaches milli-parsec separations, then gravitational wave emission becomes significant, and the binary rapidly shrinks towards the coalescence of the two BHs.

Examples of unbound BH pairs, with separations of 0.1–10 kpc, have been observed, as in the prototypical case of NGC

⋆E-mail: decarli@mpia-hd.mpg.de
†Hubble Fellow.

6240 (Komossa et al. 2003), in Arp 299 (Ballo et al. 2004), in IRAS 20210+1121 (Piconcelli et al. 2010), in Mrk 463 (Bianchi et al. 2008), in Mrk 739 (Koss et al. 2011) and in NGC 3393 (Fabbiano et al. 2012). Most of these systems show strong evidence of on-going mergers involving gas-rich galaxies, with dramatically perturbed host galaxy morphologies, intense star formation rates and high far-infrared luminosities. However, little is known about *bound* BHBs. The only spatially resolved BHB candidate to date is 0402+379, a radio galaxy with two compact cores at a projected separation of ≈7 pc (Maness et al. 2004; Rodriguez et al. 2006).

Recently, a number of BHB candidates have been identified in the Sloan Digital Sky Survey (SDSS; York et al. 2000) spectroscopic data base based on large velocity shifts (>1000 km s^{-1}) between narrow and broad emission lines (NLs and BLs, respectively). In the BHB scenario, under the assumption that one of the two BHs is active, the BLs are shifted with respect to the host galaxy rest frame (as traced by the NLs) as a consequence of the Keplerian motion of the binary (Begelman, Blandford & Rees 1980). A handful of BHB candidates have been found in this way: SDSS J092712.65+294344 (Komossa, Zhou & Lu 2008; Bogdanovic, Eracleous & Sigurdsson 2009; Dotti et al. 2009), SDSS J153636.22+044127 (Boroson & Lauer 2009), SDSS J105041.35+345631.3 (Shields et al. 2009), 4C+22.25 (J1000+2233 in this paper; Decarli et al. 2010b) and SDSS J093201.60+031858.7 (Barrows et al. 2011). More recently, we performed the first systematic search for objects with these properties in the SDSS. We used a data-driven method – heteroscedastic matrix factorization (HMF) – developed within our group (Tsalmantza & Hogg 2012). The method has been successfully applied in order to identify objects with spectroscopic features associated with two different redshift systems. Specifically, we used HMF in order to model the spectra of ∼55 000 quasars and ∼4000 galaxies and to highlight objects with shifted BLs with respect to the NLs. This search produced a list of 32 interesting objects (Tsalmantza et al. 2011). A similar systematic search has been independently performed by Eracleous et al. (2012). In this case, interesting objects were selected on the basis of anomalous profiles of the broad Hβ line, identified as outliers of principal component analysis fits of the spectra. This yielded 88 candidates, 13 of which are in common with the sample defined in Tsalmantza et al. (2011). This relatively small overlap is likely due to the different approaches followed in the two studies: the method used in Tsalmantza et al. (2011) aims at discovering objects with multiple redshift components, while the work by Eracleous et al. (2012) identifies sources with peculiar Hβ line profiles (for a more detailed comparison between these two studies, see section 3 of Eracleous et al. 2012).

The spectroscopically selected BHB candidates discussed in Tsalmantza et al. (2011) show a variety of broad line shapes, widths, luminosities, etc. This suggests that the nature of these objects is intrinsically heterogeneous. Besides the BHB scenario, velocity shifts between BLs and NLs can be attributed to the peculiar properties of the BL region of a single AGN, such as non-axisymmetric perturbations in the BL region emissivity (similar to 'hotspots' in the accretion disc), or to an edge-on disc-like geometry of the region emitting BLs, as observed in double-peaked emitters (hereafter DPEs; see e.g. Strateva et al. 2003). Alternatively, BLs and NLs may arise from two distinct sources, aligned along the line of sight. Finally, shifted BLs can be attributed to a recoiling massive BH, resulting from the coalescence of a BHB (see, e.g., Komossa et al. 2008).

The purpose of this series of papers is to test these scenarios against the BHB hypothesis for all the 32 sources in the sample identified by Tsalmantza et al. (2011). In particular, here we discuss their spectral properties (fluxes, luminosities, widths, broad line profiles and evolution). In Paper II (Lusso et al., in preparation), we study their multiwavelength spectral energy distributions. Finally, in Paper III (Decarli et al., in preparation), we analyse the images of their host galaxies and their galactic environment.

The structure of this paper is the following: in Section 2 we describe the follow-up observations and the data reduction. The analysis of the SDSS spectra and that of our second epoch data are presented in Sections 3 and 4, respectively. Discussion and conclusions are drawn in Section 5. Throughout the paper we will assume a standard cosmology with $H_0 = 70$ km s^{-1} Mpc^{-1}, $\Omega_m = 0.3$ and $\Omega_\Lambda = 0.7$.

2 OBSERVATIONAL DATA SET

Our data set consists of the SDSS spectra of the 32 sources identified in Tsalmantza et al. (2011) and of dedicated follow-up long-slit optical spectra. SDSS spectra cover the 3800–9200 Å wavelength range with a spectral resolution of $\lambda/\Delta\lambda \approx 1800$ (York et al. 2000; Abazajian et al. 2009). SDSS fibres have an aperture diameter of 3 arcsec on sky.

Follow-up observations were carried out at various facilities: Calar Alto 2.2 and 3.5 m, Lick Observatory and Keck. The journal of observations is presented in Table 1.

The bulk of the spectroscopic follow-up has been performed using the Calar Alto Faint Object Spectrograph on the 2.2 m telescope in Calar Alto. Observations were carried out with the g100 or r100 grisms, which allow a spectral resolution of $\lambda/\Delta\lambda \approx 700$ (with 1 arcsec slit) as measured from the profile of sky emission lines. The observed ranges in the two setups are 4900–7800 and 5900–9000 Å for the g100 and r100 grisms, respectively. Four sources (J0012−1022, J0927+2943, J1652+3123 and J1714+3327) were observed with the Cassegrain Twin Spectrograph at the 3.5 m telescope in Calar Alto. The T07 grism has been adopted on the red arm, providing continuous spectral coverage in the range 5500–11 000 Å with a spectral resolution of $\lambda/\Delta\lambda \approx 1300$ (1 arcsec slit). Two targets (J0155−0857 and J0221+0101) have been observed at the Lick observatory using the Kast spectrograph. Due to instrumental problems, data were collected only on the red side using the 600/7500 grating, the D55 beam splitter and the 2 arcsec slit. The two objects were observed for 1800 s in cloudy conditions and at airmasses of 1.5 and 1.3, respectively. A spectrum of the standard star G191B2B was also obtained with the same instrument configuration for flux calibration. Finally, one object, J1000+2233, has been observed while transiting at an airmass of 1.3 in non-photometric conditions with the Low Resolution Imaging Spectrometer on Keck (Oke et al. 1995). The spectrograph was configured with the 400/3400 grism, the 1200/7500 grating blazed at 9200 Å, 1 arcsec slit and the D560 dichroic. Using the 2 × 2 binning, this configuration yields a final spectral resolution of 2.1 Å pixel^{-1} in the blue and 0.8 Å pixel^{-1} in the red. Two exposures of 600 s each were acquired. The spectrophotometric star HZ44 was also observed with the same setup for flux calibration.

Standard IRAF tools were used in the reduction of Calar Alto data, in order to create master bias and flat-field images and to correct for them, to align and combine frames, perform wavelength and relative flux calibration, to perform background subtraction, and to extract 1D spectra. Multiple (three to six) frames were collected in order to easily remove cosmic rays. Sky emission lines were used in order to perform wavelength calibration. This allows us to take into account instrument flexures. The accuracy of the

Table 1. Summary of the follow-up observations. (1) Quasar name. (2) and (3) Right ascension and declination (J2000). (4) Object classification, based on the shape of Balmer lines: B – BHB candidates; D – DPEs; A – sources with Asymmetric line profiles; O – Others. (5) Redshift of narrow lines. (6) Date of spectroscopic follow-up observations. (7) Time lag between SDSS observations and our follow-up spectroscopy, in the rest frame of $z_{\rm NL}$. (8) Telescope: C2.2m = Calar Alto 2.2 m; C3.5m = Calar Alto 3.5 m; Lick; Keck. (9) Weather conditions during the spectroscopic follow-up: P = photometric; NP = not photometric; C = cloudy.

Obj. name	RA	Dec.	Class.	$z_{\rm NL}$	Date	Δt_0 (yr)	Tel.	Weather
(1)	(2)	(3)	(4)	(5)	(6)	(7)	(8)	(9)
J0012−1022	00:12:24.03	−10:22:26.3	A	0.228	2011-07-22	8.08	C3.5m	P
J0155−0857	01:55:30.02	−08:57:04.0	O	0.165	2011-09-26	8.62	Lick	C
J0221+0101	02:21:13.15	+01:01:02.9	O	0.354	2011-09-26	8.02	Lick	C
J0829+2728	08:29:30.60	+27:28:22.7	O	0.321	2012-02-22	6.32	C2.2m	NP
J0918+3156	09:18:33.82	+31:56:21.2	O	0.452	2012-02-20	5.64	C2.2m	NP
J0919+1108	09:19:30.32	+11:08:54.0	O	0.369	2012-02-20	5.86	C2.2m	NP
J0921+3835	09:21:16.13	+38:35:37.6	A	0.187	2012-02-22	7.50	C2.2m	NP
J0927+2943	09:27:12.65	+29:43:44.1	B	0.713	2012-02-20	4.14	C2.2m	NP
J0931+3204	09:31:39.05	+32:04:00.2	O	0.226	2012-02-21	5.79	C2.2m	NP
J0932+0318	09:32:01.60	+03:18:58.7	B, D	0.420	2012-02-22	7.19	C2.2m	NP
J0936+5331	09:36:53.85	+53:31:26.9	A	0.228	2011-03-15	7.48	C2.2m	C
J0942+0900	09:42:15.12	+09:00:15.8	D	0.213	2012-02-21	7.28	C2.2m	NP
J0946+0139	09:46:03.95	+01:39:23.7	A	0.220	2012-02-22	8.96	C2.2m	NP
J1000+2233	10:00:21.80	+22:33:18.6	B, D	0.419	2011-01-03	3.53	Keck	NP
J1010+3725	10:10:34.28	+37:25:14.8	O	0.282	2012-02-22	6.38	C2.2m	NP
J1012+2613	10:12:26.86	+26:13:27.3	B, D	0.378	2012-02-22	4.42	C2.2m	NP
J1027+6050	10:27:38.54	+60:50:16.5	D	0.332	2012-02-22	7.41	C2.2m	NP
J1050+3456	10:50:41.36	+34:56:31.4	B	0.272	2012-02-21	5.49	C2.2m	NP
J1105+0414	11:05:39.64	+04:14:48.2	D	0.436	2012-02-23	6.91	C2.2m	NP
J1117+6741	11:17:13.91	+67:41:22.7	O	0.248	2012-02-21	8.86	C2.2m	NP
J1154+0134	11:54:49.42	+01:34:43.6	B, A	0.469	2011-03-15	6.68	C2.2m	C
J1207+0604	12:07:55.83	+06:04:02.8	O	0.136	2012-02-23	8.69	C2.2m	NP
J1211+4647	12:11:13.97	+46:47:12.0	O	0.294	2012-02-21	6.06	C2.2m	NP
J1215+4146	12:15:22.78	+41:46:21.0	O	0.196	2012-02-21	6.55	C2.2m	NP
J1216+4159	12:16:09.60	+41:59:28.4	O	0.242	2012-02-22	6.31	C2.2m	NP
J1328−0129	13:28:34.15	−01:29:17.6	O	0.151	2012-02-20	8.45	C2.2m	NP
J1414+1658	14:14:42.03	+16:58:07.2	O	0.237	2012-02-23	3.23	C2.2m	NP
J1440+3319	14:40:05.31	+33:19:44.5	A	0.179	2012-02-23	5.77	C2.2m	NP
J1536+0441	15:36:36.22	+04:41:27.0	B, D	0.389	2012-02-23	2.78	C2.2m	NP
J1539+3333	15:39:08.09	+33:33:28.0	B	0.226	2011-03-12	6.28	C2.2m	C
J1652+3123	16:52:55.90	+31:23:43.8	O	0.593	2011-07-23	5.12	C3.5m	P
J1714+3327	17:14:48.51	+33:27:38.3	B, O	0.181	2011-07-21	2.72	C3.5m	P

wavelength calibration is typically of $\lesssim$1 Å (residual rms) over the whole observed range. This corresponds to minimum velocity uncertainties of $\sim$40 km s^{-1}, if we observe a line at 5000 Å (rest frame) shifted to a fiducial redshift $z = 0.4$ (much smaller than typical uncertainties in the fit of broad line peak wavelengths, see Section 4). Relative flux calibration was performed using the spectra of spectrophotometric standards, e.g. Feige56, Feige66, BD+75° 325, BD+33° 2642. A similar procedure was adopted during the reduction of the Lick and Keck data using the LowRedux pipeline (http://www.ucolick.org/~xavier/LowRedux/index.html). Since observations were mostly performed under non-photometric conditions, absolute flux calibration is uncertain. Since we are mostly interested in the evolution of the profiles of BLs, we scaled the spectra so that the fluxes of the [O III] and [N II] narrow lines in our spectra match the ones observed in the SDSS data. The median correction corresponds to a factor of $\sim$1.4.

3 SPECTRAL PROPERTIES

In order to study the emission line properties of these sources, we model and subtract the continuum emission following a procedure similar to the one presented in Decarli et al. (2010a) and De Rosa et al. (2011). Namely, the continuum emission is fitted with a superposition of a power law, a Balmer pseudo-continuum (Grandi 1982), a host galaxy model (here we refer to the templates by Kinney et al. 1996) and an Fe II template (adapted from Verner et al. 2009). An example of continuum modelling is shown in Fig. 1.

A variety of line profiles were reported in our original SDSS-based selection. We introduce the following basic classification scheme: fairly bell-shaped, strongly shifted broad lines (e.g. in J0927+2943, J1539+3333, J1714+3327) identify good BHB candidates (although the BHB scenario does not necessarily imply a Gaussian line profile, see e.g. Bogdanovic et al. 2008; Shen & Loeb 2010); very broad lines with tentative evidence of double-horned profiles are labelled as DPEs (e.g. in J1012−2613, J1027+6050, J1105+0414); lines showing a rather symmetric base, centred at the redshift of the narrow lines, but an asymmetric core, resulting in a shifted peak, are called 'Asymmetric' (e.g. in J0012−1022, J0936+5331, J0946+0139); and other, more complex profiles (e.g. J1010+3725, J1215+4146, etc.) or lines with relatively small velocity shifts or asymmetric wings but modest peak shift are referred to

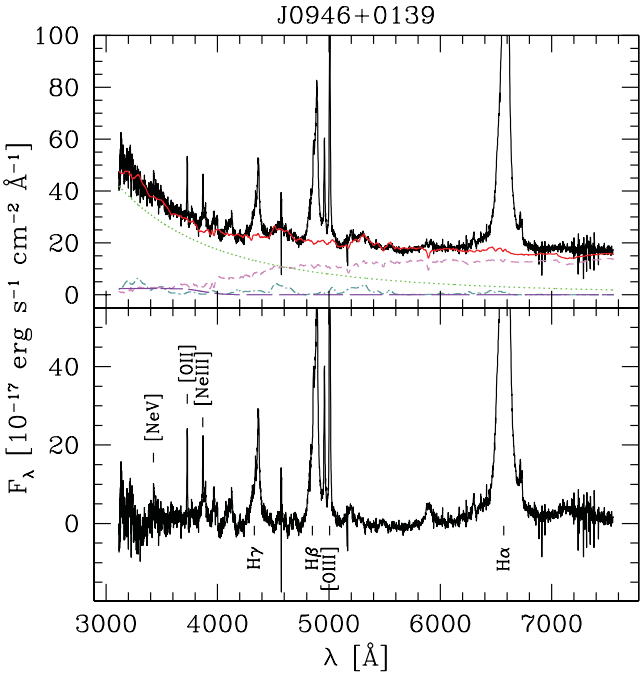

Figure 1. Example of continuum decomposition. Top panel: SDSS spectrum of J0946+0139. The dotted, dash–dotted, short-dashed and long-dashed lines show the power law, the Fe II template, the host galaxy template and the Balmer pseudo-continuum. The total fit is also shown as a red solid line. Bottom panel: residual spectrum. Main emission lines are also labelled.

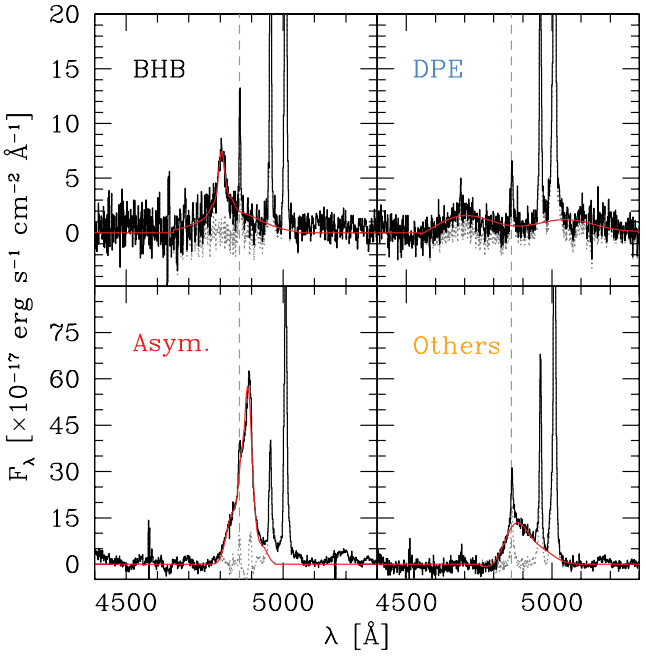

Figure 2. Examples of the broad line profiles in each class of objects in our sample. We label as 'BHB candidates' objects with fairly symmetric broad line profiles, with clear shifts (>1000 km s^{-1}) with respect to their narrow components (here, J1050+3456); as 'DPE candidates' objects which show a double-horned profile of broad lines (in this figure, J1000+2233); as 'Asymmetric' objects in which the broad lines have a symmetric base but a highly skewed, asymmetric core (here, J0946+0139); and as 'Others' sources with small shifts or irregular line profiles (here, J1414+1658). In the plots, we show the observed SDSS spectra around the Hβ region (solid black line), after the continuum emission has been modelled out and subtracted (see the text for details) and after shifting the spectra back to the rest frame (based on $z_{\rm NL}$; see Table 1). The dashed vertical lines mark the narrow component of Hβ. The red lines show the fit to the broad component of Hβ. Residuals are plotted with grey dotted lines.

as 'Others'. Fig. 2 shows a prototypical example for each class of objects.[1]

We focus on the properties of Hβ, [O II], [O III], [Ne III] and [Ne V], which are all covered in the SDSS spectra of all the sources in our sample, and of Hα when available. The Hβ broad component is modelled with a superposition of a series of Gauss–Hermite polynomials (up to the seventh order), plus a Gaussian curve. These components are required in order to reproduce the complex line profiles of the sources in our sample. Examples of line fits are shown in Fig. 2. For all the other lines, we compute fluxes and peak wavelengths as zeroth and first moments of the observed lines, and the line widths as full widths at half-maximum (FWHM) directly measured on the observed line profiles. Typical uncertainties are $\sim$0.1 and $\sim$0.15 dex in the luminosity and widths of broad lines (mostly due to model degeneracies and fit residuals), and of $\sim$0.05 dex in the widths of narrow lines (dominated by the noise in the data). Tables 2 and 3 summarize the properties of these lines in each source.

The sources in our sample have been selected because they show two redshift systems at $z_{\rm NL}$ and $z_{\rm BL}$. In 20 cases out of 32, $z_{\rm NL} < z_{\rm BL}$.[2] Narrow [O III] emission is observed at both $z_{\rm NL}$ and $z_{\rm BL}$ in only two cases, J0927+2943 and J1539+3333, both of which are considered BHB candidates in this analysis (see Fig. 3). The former source shows also [O II], [Ne III] and [Ne V] emission at both redshifts, implying AGN-like ionization conditions of the gas emitting the two sets of lines (see also Komossa et al. 2008). For J1539+3333, no clear indication of [Ne V] is observed at any redshift (for a discussion on how a second system of narrow lines can be interpreted in the light of the BHB hypothesis, see Bogdanovic et al. 2009; Dotti et al. 2009). Finally, the [O III] lines of J1010+3725 show broad profiles with multiple components at various velocities, likely caused by massive gaseous outflows driven either by star formation or AGN winds. Such a feature is not observed in other, lower ionization lines (e.g. [O II]). All the remaining sources show only one set of NLs. High-ionization lines (including [Ne III] and [Ne V]) are ubiquitously reported.

Fig. 4 shows various gas diagnostics based on the luminosities and widths of both NLs and BLs. The luminosities of [O III] and Hβ (broad) are highly correlated, as generally observed in normal quasars (Shen et al. 2011), with L(Hβ,B) = 1–10 × L([O III]). Largest deviations (e.g. the clear outlier J1215+4145) seem to be associated with high Hα,B/Hβ,B ratios. DPEs in our sample tend to show bright [O III] and broad Hβ emission (L(Hβ,B) $>10^{42}$ erg s^{-1}), with line widths >8000 km s^{-1}. Given that L(Hβ,B) is proportional to the continuum luminosity, which is a proxy of the size of the BL region (Bentz et al. 2010), it is implied that, at face value, virial estimates of the BH mass in DPEs are large ($>10^9$ M$_\odot$; for a discussion on the limitations of these estimates, see

[1] We note that this classification scheme is not univocal. The ambiguity may be observational (poor S/N, or line wings overlapping on to other spectral features) or due to the fact that the classes used here are not mutually exclusive, e.g. some DPEs have broad line profiles similar to the 'Asymmetric' ones.

[2] The small asymmetry between the number of blue and redshifted BLs may be explained by the contamination of the [O III] lines, which may hinder the identification of redshifted, weak and broad Hβ emission lines.

Table 2. Line luminosities of [Ne v], [Ne iii], [O ii], [O iii], broad Hβ and Hα as measured from the SDSS spectra.

Obj. name (1)	L ([Ne v]) (10^{41} erg s^{-1}) (2)	L ([Ne iii]) (10^{41} erg s^{-1}) (3)	L ([O ii]) (10^{41} erg s^{-1}) (4)	L ([O iii]) (10^{41} erg s^{-1}) (5)	L (Hβ, B) (10^{41} erg s^{-1}) (6)	L (Hα, B) (10^{41} erg s^{-1}) (7)
J0012−1022	0.34 ± 0.35	1.46 ± 0.19	1.97 ± 0.21	7.79 ± 0.19	34.59 ± 3.46	96.84 ± 3.46
J0155−0857	1.12 ± 0.21	2.03 ± 0.14	1.42 ± 0.15	4.83 ± 0.19	32.25 ± 3.22	92.28 ± 3.22
J0221+0101	2.59 ± 0.32	2.12 ± 0.21	1.73 ± 0.22	6.70 ± 0.22	25.18 ± 2.52	54.18 ± 2.52
J0829+2728	3.03 ± 0.33	3.77 ± 0.23	3.64 ± 0.25	9.97 ± 0.30	16.54 ± 1.65	49.60 ± 1.65
J0918+3156	2.82 ± 0.56	10.22 ± 0.58	16.32 ± 0.67	38.80 ± 0.84	124.46 ± 12.45	–
J0919+1108	15.24 ± 1.71	8.48 ± 1.11	2.41 ± 0.53	22.75 ± 0.59	103.43 ± 10.34	–
J0921+3835	1.31 ± 0.39	0.27 ± 0.11	1.10 ± 0.14	7.57 ± 0.17	17.93 ± 1.79	51.76 ± 1.79
J0927+2943	2.91 ± 2.26	7.51 ± 1.04	23.25 ± 1.23	35.44 ± 2.20	93.99 ± 9.40	–
J0931+3204	2.77 ± 0.28	1.39 ± 0.11	0.33 ± 0.08	5.62 ± 0.14	4.94 ± 0.49	28.26 ± 0.49
J0932+0318	4.60 ± 0.77	3.95 ± 0.56	4.66 ± 0.49	13.30 ± 0.49	39.95 ± 3.99	–
J0936+5331	2.02 ± 0.32	3.10 ± 0.20	0.55 ± 0.15	7.76 ± 0.22	58.87 ± 5.89	163.95 ± 5.89
J0942+0900	2.29 ± 0.37	3.69 ± 0.21	5.43 ± 0.27	14.93 ± 0.30	24.46 ± 2.45	62.86 ± 2.45
J0946+0139	0.98 ± 0.12	3.45 ± 0.11	2.03 ± 0.10	7.48 ± 0.11	30.55 ± 3.05	101.07 ± 3.05
J1000+2233	7.86 ± 0.65	3.74 ± 0.37	7.24 ± 0.42	20.58 ± 0.58	23.91 ± 2.39	–
J1010+3725	0.50 ± 0.35	4.31 ± 0.22	6.35 ± 0.26	34.76 ± 0.32	16.47 ± 1.65	–
J1012+2613	5.47 ± 0.48	4.56 ± 0.39	3.86 ± 0.26	21.08 ± 0.37	20.40 ± 2.04	–
J1027+6050	4.48 ± 1.05	0.80 ± 0.42	2.45 ± 0.49	7.10 ± 0.44	49.53 ± 4.95	80.24 ± 4.95
J1050+3456	0.72 ± 0.25	1.32 ± 0.16	3.32 ± 0.19	4.33 ± 0.24	7.57 ± 0.76	26.63 ± 0.76
J1105+0414	4.65 ± 0.72	3.66 ± 0.52	4.06 ± 0.63	22.84 ± 0.66	109.16 ± 10.92	–
J1117+6741	2.35 ± 0.39	0.88 ± 0.17	2.54 ± 0.13	4.92 ± 0.12	3.36 ± 0.34	16.05 ± 0.34
J1154+0134	0.65 ± 0.96	2.08 ± 0.73	9.73 ± 0.84	15.47 ± 0.78	52.47 ± 5.25	–
J1207+0604	0.74 ± 0.09	0.41 ± 0.04	0.30 ± 0.05	1.72 ± 0.06	4.20 ± 0.42	12.78 ± 0.42
J1211+4647	3.56 ± 0.44	3.47 ± 0.28	1.35 ± 0.21	9.62 ± 0.23	19.71 ± 1.97	78.66 ± 1.97
J1215+4146	0.54 ± 0.16	1.83 ± 0.10	3.26 ± 0.12	11.87 ± 0.18	1.36 ± 0.14	32.68 ± 0.14
J1216+4159	1.26 ± 0.16	2.44 ± 0.16	3.18 ± 0.19	6.96 ± 0.23	4.58 ± 0.46	28.09 ± 0.46
J1328−0129	0.93 ± 0.09	1.14 ± 0.06	1.37 ± 0.06	3.64 ± 0.11	3.79 ± 0.38	22.33 ± 0.38
J1414+1658	3.61 ± 0.25	5.91 ± 0.17	3.15 ± 0.15	15.37 ± 0.19	17.94 ± 1.79	65.20 ± 1.79
J1440+3319	0.47 ± 0.16	0.46 ± 0.08	1.21 ± 0.10	3.33 ± 0.11	3.15 ± 0.32	16.44 ± 0.32
J1536+0441	4.11 ± 0.64	5.89 ± 0.51	3.05 ± 0.61	26.87 ± 0.73	95.49 ± 9.55	–
J1539+3333	0.12 ± 0.16	0.01 ± 0.10	1.13 ± 0.12	0.37 ± 0.09	1.56 ± 0.16	4.56 ± 0.16
J1652+3123	9.55 ± 1.85	17.38 ± 1.42	14.41 ± 1.51	59.45 ± 1.90	208.83 ± 20.88	–
J1714+3327	0.81 ± 0.22	3.53 ± 0.14	0.80 ± 0.13	11.59 ± 0.15	27.48 ± 2.75	88.43 ± 2.75

Wu & Liu 2004; Lewis & Eracleous 2006). Asymmetric broad lines tend to show bright BLs with L(Hβ,B) $>10^{42}$ erg s^{-1} and intermediate-to-high L(Hβ,B)/L([O iii]) ratios, and relatively modest (2500–5000 km s^{-1}) widths. The only exception is J1440+3319, which shows significantly lower BL luminosity (L(Hβ,B) = 3.2 × 10^{41} erg s^{-1}) but high Hα,B/Hβ,B (5.2 instead of ∼3 as observed in all the other asymmetric objects). BHB candidates and sources listed as 'Others' show a broad range of broad line luminosities and widths. The majority (27/32) of our sources show typical AGN-like ionization conditions (see, for instance, Groves et al. 2004a,b), as traced by the [O iii]/[O ii] versus [Ne v]/[Ne iii] diagnostic (due to its high ionization energy, [Ne v] cannot be photoionized by star formation only). A handful of sources show [Ne v]/[Ne iii] values exceeding unity, which is not typically observed in lower luminosity AGN (Groves et al. 2004a,b). This suggests a complete ionization of the clouds in the NL region. Among the targets without clear AGN-like ionization conditions, three are BHB candidates (J1050+3456, J1154+0134 and J1539+3333), one is an object with asymmetric line profiles (J0012−1022) and one was classified as 'Others' (J1010+3725). Finally, when comparing the FWHM values of [O iii] and [O ii], we find a wide range of NL widths, from practically unresolved (the BHB candidates J0927+2943 and J1050+3456, or the source J0155−0857) to extremely broad (e.g. J0931+3204 and J1010+3725, with FWHM$_{[O\,III]}$ > 1000 km s^{-1}).

4 BROAD LINE TEMPORAL EVOLUTION

A key prediction of the BHB scenario is that the peaks of BLs should shift periodically from longer to shorter wavelengths (and vice versa) with respect to NLs, over orbital periods which are estimated to be 1–500 yr for the most reasonable geometrical configurations and BH masses (see Fig. 5, left, and Dotti et al. 2009; Lauer & Boroson 2009).

Variations in the profiles of BLs have been observed in several AGN. A clear-cut example is the evolution of the Hβ line profile in NGC 5548 over 30 yr (Sergeev et al. 2007),[3] where blue- and redshifted peaks or double-horned profiles are observed for the same object in different epochs. Usually these features have modest entity (e.g. peak shifts $\Delta v \lesssim 500$ km s^{-1}) evolve irregularly and dissipate out in less than an orbital period of the BL region. The generally accepted picture is that they arise in dynamically unstable 'bright spots' of the BL region.

Monitoring the evolution of BL profiles over 5–10 yr (i.e. a significant fraction of the BL region orbital period) is required in order to distinguish between the BHB hypothesis and other scenarios. If the shifted peaks of BLs change their fluxes or

[3] For an animation of the line profile evolution, see http://www.astronomy.ohio-state.edu/~peterson/AGN/30year.avi

Table 3. Line widths of [O II], [O III] and of the broad component of Hβ in the targets of our sample.

Obj. name	FWHM (km s^{-1})		
	[O II]	[O III]	Hβ, B
(1)	(2)	(3)	(4)
J0012−1022	400	480	4500
J0155−0857	440	300	7300
J0221+0101	440	330	7100
J0829+2728	440	420	5300
J0918+3156	640	570	6700
J0919+1108	560	840	7900
J0921+3835	480	600	3100
J0927+2943	440	240	6200
J0931+3204	320	1050	3800
J0932+0318	480	480	11 800
J0936+5331	400	540	4700
J0942+0900	480	570	22 000
J0946+0139	520	570	2700
J1000+2233	480	420	23 000
J1010+3725	640	1140	2000
J1012+2613	480	630	19 000
J1027+6050	400	360	29 000
J1050+3456	480	300	2900
J1105+0414	560	510	27 000
J1117+6741	560	480	7100
J1154+0134	480	570	4200
J1207+0604	440	330	11 400
J1211+4647	480	600	5400
J1215+4146	640	750	3600
J1216+4159	480	420	13 000
J1328−0129	560	360	10 600
J1414+1658	480	480	6900
J1440+3319	560	390	6900
J1536+0441	640	600	2300
J1539+3333	480	420	1300
J1652+3123	400	660	10 100
J1714+3327	560	660	4800

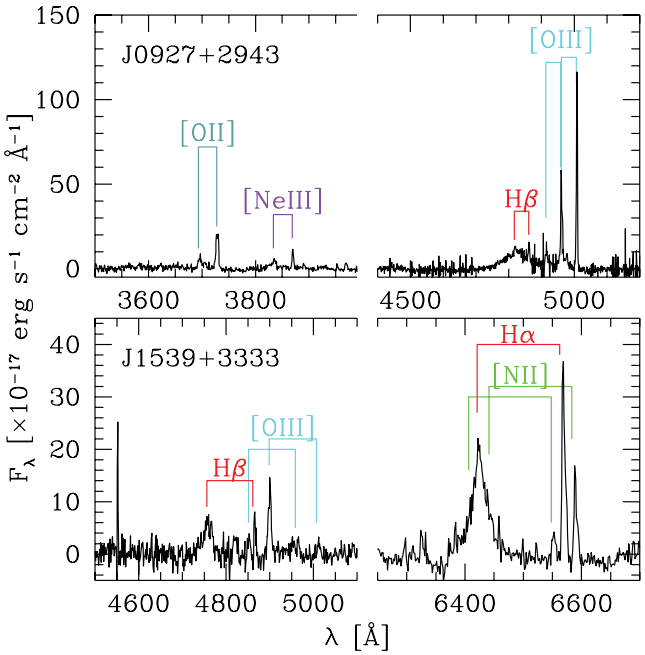

Figure 3. Continuum-subtracted SDSS spectra of J0927+2943 and J1539+3333. Both spectra show two sets of narrow lines, the most prominent of which are labelled.

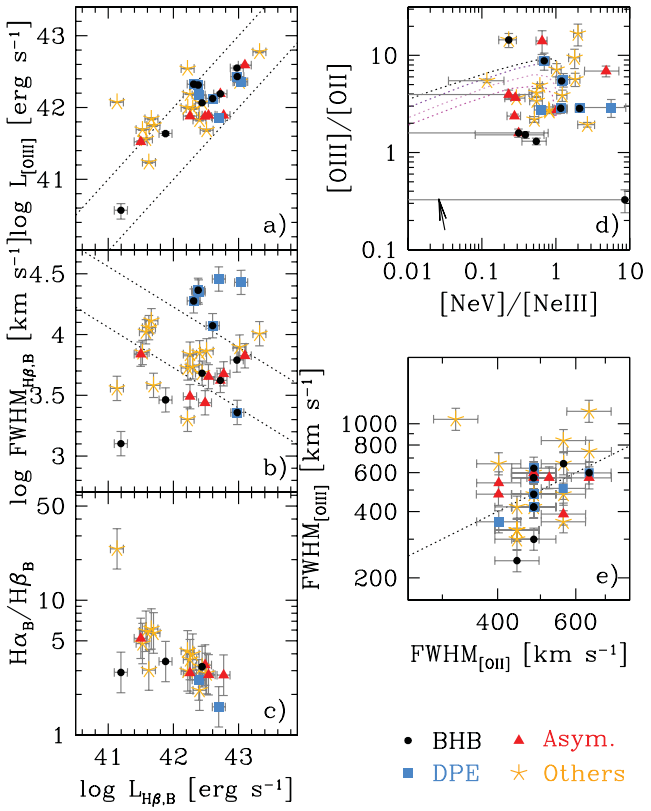

Figure 4. Narrow and broad line diagnostics. The black, blue, red and yellow symbols mark BHB candidates, DPEs, objects with asymmetric line profiles and other sources, respectively. (a) Comparison between Hβ (broad) and [O III] luminosities. The dotted lines show the cases L(Hβ) = 1–10 L([O III]). (b) Width versus luminosity of broad Hβ. The dotted lines mark the loci of virial BH masses equal to 10^9 and 10^8 $M_\odot$. (c) Flux ratio between the broad components of Hα and Hβ, as a function of L(Hβ). (d) [O III]/[O II] versus [Ne V]/[Ne III] diagnostic of the gas ionization in the interstellar medium. The dotted lines show the expected values for AGN-like ionization conditions at various spectral indices (different curves; from dark to bright colours at increasing spectral steepness) and ionization parameters (increasing from left to right). The arrow shows the effects of $A_V = 2$ mag reddening. Adapted from Groves, Dopita & Sutherland (2004a,b). (e) Comparison between the widths of [O III] and [O II] (considered as a single line, as the doublet cannot be resolved in any of these sources). The dotted line shows the one-to-one case.

shapes, without any predictable behaviour (in particular, with no periodic behaviour), then the 'bright-spot' scenario is favoured. In contrast, if the peak shifts periodically around the NL redshift over several periods, then the BHB interpretation would be confirmed.

In order to quantify the evolution in the line profiles, we first fit the peak of each BL with a single Gaussian. Compared to the fitting method described in Section 3, this approach performs better in identifying the peak wavelength in the case of steep profiles (as observed in a number of our sources), whereas the Gauss–Hermite approach provides a better description of the overall line properties. We perform this analysis on both our follow-up data and the SDSS spectra. Our measurements of the peak velocity differences, their uncertainties and the corresponding mean accelerations are reported in Table 4 and plotted in Fig. 5 (right). Velocity shifts are computed on the Hα profiles, unless only Hβ is available. Prominent

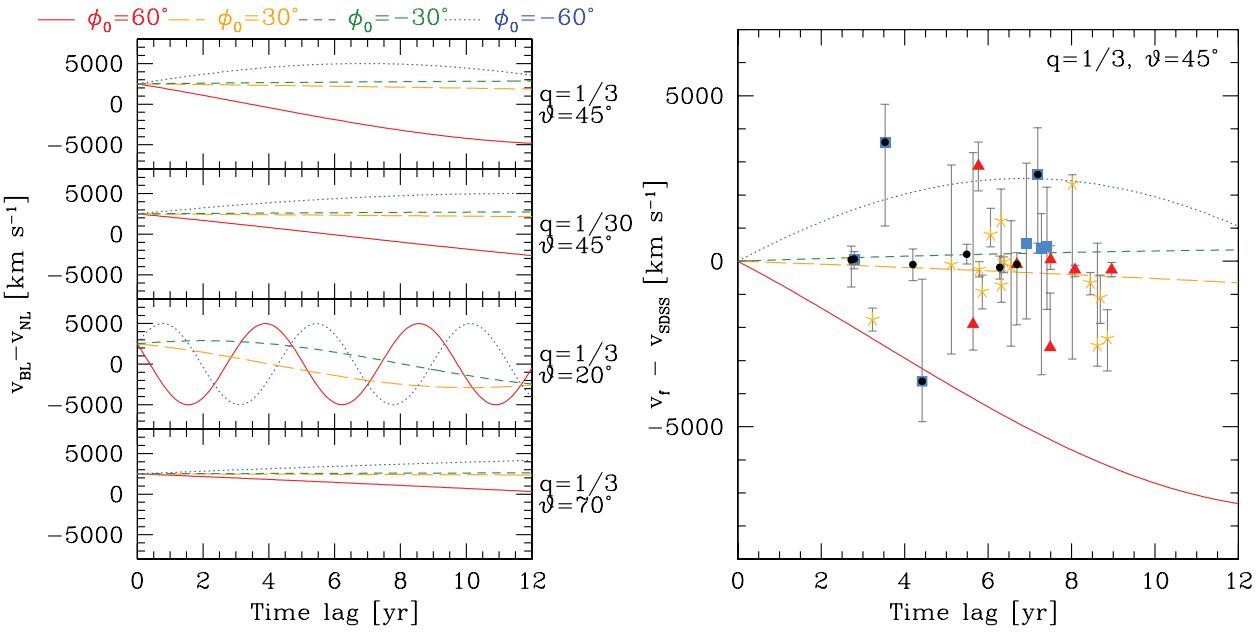

Figure 5. Left: expected evolution of the observed velocity shift for a BHB with primary BH mass $M_1 = 10^9$ M$_\odot$, initial velocity shift between BLs and NLs of 2500 km s^{-1}, and various values of the BH mass ratio $q = M_2/M_1$, of the inclination angle of the orbit plane ϑ, and of the initial phase ϕ_0. Right: the observed difference between the BL peak shifts in our follow-up spectra (v_f) and in SDSS data. The colour code highlights the source classification, as in Fig. 4. For a comparison, we overplot the expected evolution predicted in the case of $M_1 = 10^9$ M$_\odot$, $q = 1/3$, $\vartheta = 45°$, assuming various orbital phases of the binary at the time of the SDSS observations.

($> 2\sigma$) changes in the BL peak wavelengths are reported in five sources: J1117+6741, J1211+4647, J1328−0129, J1414+1658 (all classified as 'Others') and J1440+3319 ('Asymmetric'). Less significant changes are also reported for the 'Asymmetric' sources J0012−1022 and J0936+5331, and for J1207+0604 (classified as 'Others').

We note however that the changes in the peak wavelengths reported here may be part of a more general evolution in the line profile, which may not be associated with, e.g., a BHB. As a matter of fact, the general phenomenology of the line profile evolution is more complex. For instance, the spectrum of J1414+1658 shows a clear change both in the peak wavelength and in the flux of the BLs. In J1328−0129, the evolution in the BL shift is associated with the appearance of a new peak in the Hα line profile at $\lambda \sim 6490$ Å, while the base of the line profile remained unchanged. The Hβ and Hα lines in the J1207+0604 spectrum became more extended bluewards, and the line profile more boxy. In Figs 6–8, we compare the continuum-subtracted line profiles of Hα and Hβ observed in SDSS data with those in our follow-up spectra, by plotting the normalized difference between the observed BL profiles: [F_λ(follow-up) − F_λ(SDSS)]/F_λ(SDSS). In order to regularize this ratio, at the denominator we use the BL model of SDSS lines obtained in Section 3, instead of the observed profile, and we bin into 10 Å intervals, to ease the visualization of small variations in regimes of modest signal-to-noise.

Significant line profile temporal variations are reported in 11 out of 32 sources. In eight of them (J0012−1022, J0936+5331, J1117+6741, J1207+0604, J1211+4647, J1328−0129, J1414+1658, J1440+3319), the profile of BLs changed in shape, with asymmetric features appearing or disappearing, shifts in the peak wavelengths, etc. In the remaining three sources (J0221+0101, J0918+3156, J1216+4159) we observe a significant (>30 per cent) drop in the flux of BLs with no clear indication of a variation of the peak wavelength. Minor (∼10 per cent) flux variations are also reported in additional five sources (J0932+0318, J0942+0900, J0946+0139, J1050+3456 and J1536+0441). A short description of the most prominent variations in the BL profiles observed in this study is given in Appendix A.

As final remarks: (i) for one object (J0155−0857) the poor quality of our follow-up observations hinders any conclusive statements about the evolution of the line profiles. (ii) J1000+2233 does not show any variation in the Hα profile (the Hβ line is not covered by our follow-up). However, our Keck spectrum of this quasar covers for the first time the red wing of Hα and the blue wing of Mg II (see Fig. 9). The former shows an 'M'-shaped profile, while the latter is fairly bell shaped with significant smaller velocity shift compared with the blue peak of Balmer lines, suggesting that this source is a DPE.

5 DISCUSSION AND CONCLUSIONS

In this paper we investigate the nature of BHB candidates selected based on velocity shifts between broad and narrow lines in their SDSS spectra. According to the profiles of BLs, we divided the sample into four classes: BHB candidates, showing fairly symmetric line profiles and big (>1000 km s^{-1}) velocity shifts; DPEs, with very broad lines, possibly showing double-horned profiles; objects with Asymmetric lines; and other sources, showing irregular line profiles, or modest shifts (∼1000 km s^{-1}) between BLs and NLs.

The analysis of the SDSS discovery spectra reveals the following facts.

(1) BHB candidates cover a wide range in terms of broad and narrow line luminosities, widths and virial estimates of the BH mass. DPEs tend to show very bright and broad lines (yielding large

Table 4. Evolution of the shift of broad line peaks between SDSS and our follow-up observations, and corresponding (rest-frame) mean acceleration.

Obj. name	$\Delta v_{\rm BL}$ (km s^{-1})	Acceleration (km s^{-1} yr^{-1})
(1)	(2)	(3)
J0012−1022	-260^{+130}_{-210}	-32^{+17}_{-26}
J0155−0857	-2500^{+3100}_{-600}	-295^{+360}_{-70}
J0221+0101	$+2300^{+300}_{-5300}$	$+290^{+30}_{-660}$
J0829+2728	-720^{+620}_{-520}	-110^{+100}_{-80}
J0918+3156	-1900^{+5200}_{-800}	-340^{+920}_{-140}
J0919+1108	-900^{+500}_{-500}	-160^{+80}_{-90}
J0921+3835	$+50^{+420}_{-300}$	$+10^{+60}_{-40}$
J0927+2943	-100^{+500}_{-500}	-20^{+110}_{-120}
J0931+3204	-240^{+220}_{-230}	-40^{+40}_{-40}
J0932+0318	$+2600^{+1400}_{-2100}$	$+360^{+200}_{-290}$
J0936+5331	-2600^{+1600}_{-100}	-350^{+220}_{-10}
J0942+0900	$+400^{+1100}_{-3800}$	$+50^{+140}_{-520}$
J0946+0139	-260^{+220}_{-210}	-30^{+25}_{-25}
J1000+2233	$+3600^{+1100}_{-2500}$	$+1000^{+300}_{-700}$
J1010+3725	0^{+130}_{-350}	0^{+20}_{-55}
J1012+2613	-3600^{+3100}_{-1200}	-820^{+700}_{-280}
J1027+6050	$+400^{+1800}_{-1900}$	$+60^{+240}_{-250}$
J1050+3456	$+210^{+300}_{-300}$	$+40^{+55}_{-55}$
J1105+0414	$+550^{+2400}_{-2300}$	$+80^{+350}_{-330}$
J1117+6741	-2300^{+900}_{-1000}	-260^{+100}_{-110}
J1154+0134	-100^{+400}_{-1800}	-15^{+55}_{-275}
J1207+0604	-1100^{+700}_{-800}	-130^{+80}_{-90}
J1211+4647	$+800^{+790}_{-370}$	$+130^{+130}_{-60}$
J1215+4146	-150^{+1400}_{-2400}	-20^{+210}_{-370}
J1216+4159	$+1200^{+1000}_{-1400}$	$+190^{+150}_{-220}$
J1328−0129	-650^{+310}_{-370}	-80^{+40}_{-40}
J1414+1658	-1800^{+350}_{-350}	-540^{+110}_{-110}
J1440+3319	$+2900^{+730}_{-750}$	$+500^{+130}_{-130}$
J1536+0441	$+70^{+230}_{-290}$	$+20^{+80}_{-110}$
J1539+3333	-190^{+350}_{-350}	-30^{+55}_{-55}
J1652+3123	-100^{+3000}_{-2700}	-20^{+590}_{-530}
J1714+3327	$+50^{+420}_{-820}$	$+20^{+150}_{-300}$

virial BH mass estimates), the only exception being the BHB/DPE candidate J1536+0441 (Boroson & Lauer 2009), which shows a modest FWHM for the broad component of Hβ. Asymmetric BLs tend to show bright BL luminosities and relatively high [O III] widths (FWHM$_{[\rm O\,III]} \sim 500$ km s^{-1}). Remaining sources tend to have intermediate-to-low line luminosities and virial BH masses $<10^9$ M$_\odot$. Some of these sources show high Hα/Hβ flux ratios in the broad components of their lines. In a few cases, NLs are significantly broadened (FWHM$_{[\rm O\,III]} > 800$ km s^{-1}).

(2) For the majority of the sources, ionization properties in the NL region are consistent with what is typically observed in quasars. In particular, hard radiation fields are needed to explain the generally high [Ne V]/[Ne III] ratios observed in our sources. Only a handful of targets (all classified as 'BHB', 'Asymmetric' or hybrid candidates) have modest or no [Ne V] emission, and may not require AGN-like ionization conditions.

(3) Two sources (J0927+2943 and J1539+3333) show two sets of narrow lines, both at $z_{\rm NL}$ and at $z_{\rm BL}$. Another source (J1010+3725) shows broadened, multicomponent narrow lines. All the remaining sources show no NLs at the redshift of the BLs. Ionization conditions of the secondary set of NLs in J1010+3725 and J1539+3333 suggest modest or no AGN contribution; this is not the case for J0927+2943, which shows [Ne V] emission at both $z_{\rm NL}$ and $z_{\rm BL}$.

By comparing the SDSS spectra with our second epoch spectra we found the following.

(1) 16 out of 32 objects did not undergo any significant evolution in their broad line profiles or flux over a (rest-frame) time-scale of 2–10 yr.

(2) Minor flux variations are reported in five targets, with no appreciable change in the line profile.

(3) Three sources (J0221+0101, J0918+3156, J1216+4159) show conspicuous variations in the BL fluxes (>30 per cent), but with no clear change in the shape of the line profiles.

(4) Eight sources show significant evolution in the light profile, in diverse forms. In particular, the BL peak wavelength shifted in five sources, although such an evolution may be ascribed to a more general change in the shape of the line profile.

(5) Some degree of evolution in the line profiles is common in objects with asymmetric lines (4 out of 5) and in 'Other' sources (8 out of 15), while is less frequent in BHB candidates (including hybrid classifications, only 3 sources out of 9 show some modest flux variation, and none of them show any significant shift in the BL peak wavelength) and in DPEs (1 out of 3). All the shifts in the BL peaks are associated with a general change of the whole BL profile, rather than with a 'rigid' shift of the line.

The absence of a clear shift in the majority of the objects (in particular, in those identified as BHB candidates) does not rule out a BHB explanation. Small to negligible differences in the peak position are expected for various plausible configurations, in particular if the binary orientation is such that it maximizes the projected velocity shift (i.e. minimizes the acceleration component along the line of sight; see Fig. 5, left). On the other hand, fast evolution of the Balmer lines (likely associated with boxy profiles) is one of the predicted signatures of close and short period BHBs (Bogdanovic et al. 2008; Shen & Loeb 2010). It is still unclear whether the variability observed in our sample is associated with BHBs or with bright spots in the BL region of 'normal' AGN. Since changes in the BL peak wavelengths seem to be exclusively associated with dramatic fluctuations in line luminosities, with relatively modest peak velocity changes, the BHB scenario is likely disfavoured for these sources. Theoretically, in the BHB scenario the luminosity of the secondary is expected to evolve over a time-scale comparable with the orbital period of the binary (Artymowicz & Lubow 1994; Hayasaki, Mineshige & Ho 2008; Roedig et al. 2011, 2012; Sesana et al. 2012, although fast fluctuations in the BH light curves on very short time-scales would not be temporarily resolved by the numerical simulations cited above). New observations in 1–5 yr time lags will allow us to assess whether the variations observed so far are transient features (as expected in the bright-spot scenario) or follow a regular evolution (as predicted in the BHB hypothesis).

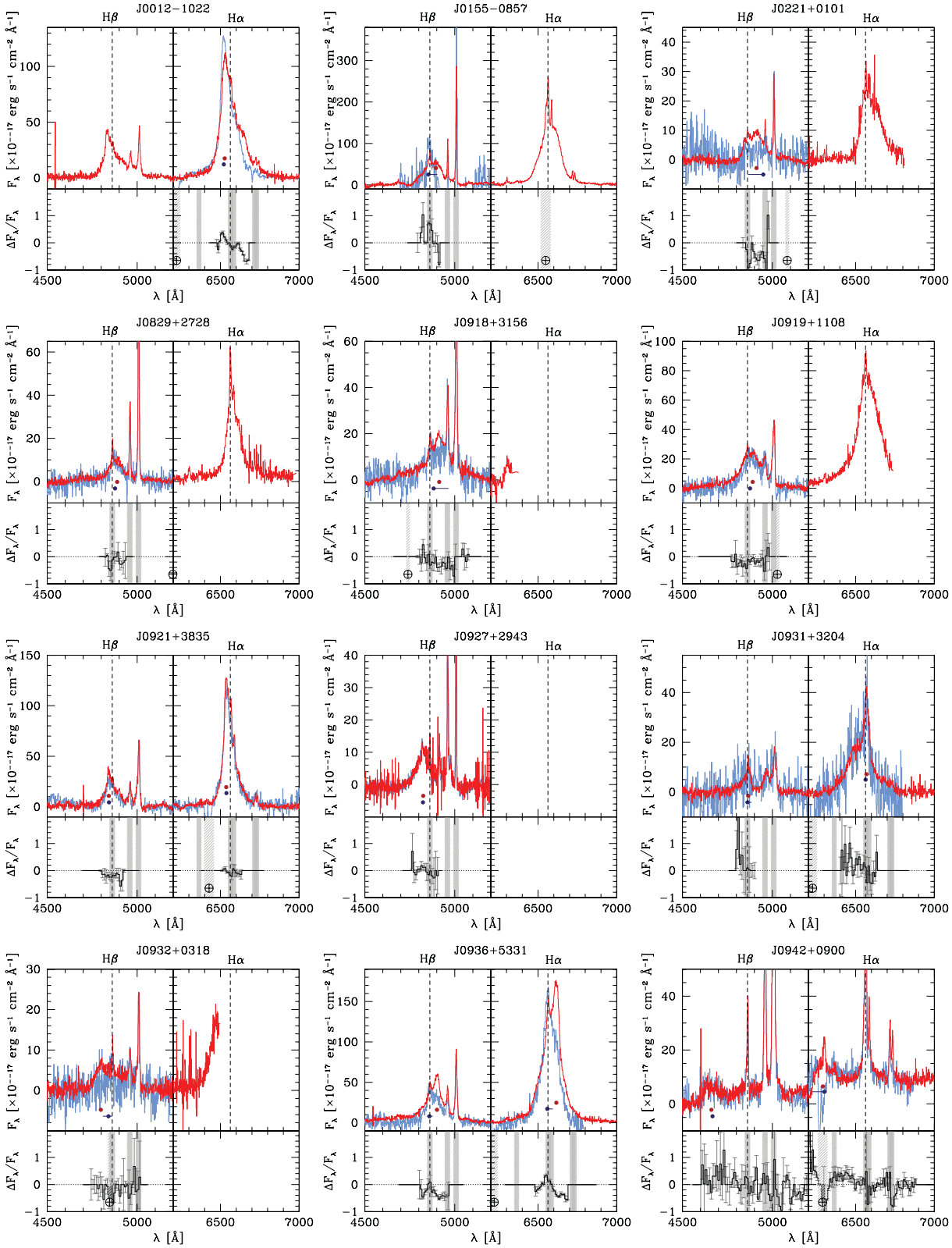

Figure 6. Comparison between the SDSS data and our follow-up observations for the quasars in our sample. The top panels of each window show the Hβ (left) and Hα (right) line profiles in the SDSS spectrum (red) and in our follow-ups (blue). Spectra have been continuum subtracted, and scaled so that the [O III] and [N II] lines in the follow-up observations match the flux observed in the SDSS spectra (see the text for details). The expected wavelengths of the narrow components of Hα and Hβ are highlighted with dashed vertical lines, while the observed BL peak wavelengths are marked with dark red and blue points. The bottom panels show the difference between the two epochs, normalized to the BL fit of the SDSS data and resampled in 10 Å wide bins for the sake of clarity. The grey shaded areas mark the position of prominent NLs and of atmospheric absorption features.

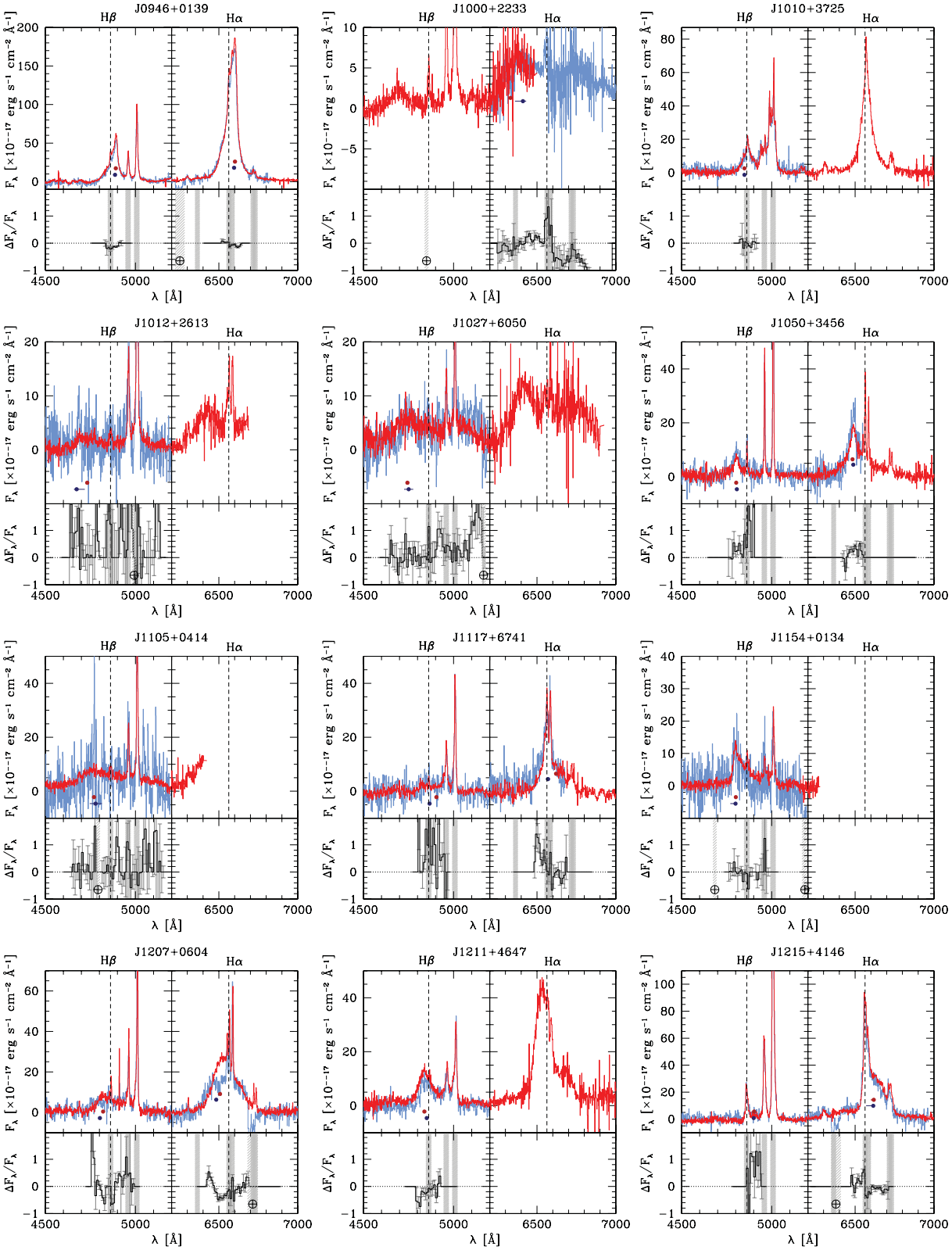

Figure 7. Continuation from Fig. 6.

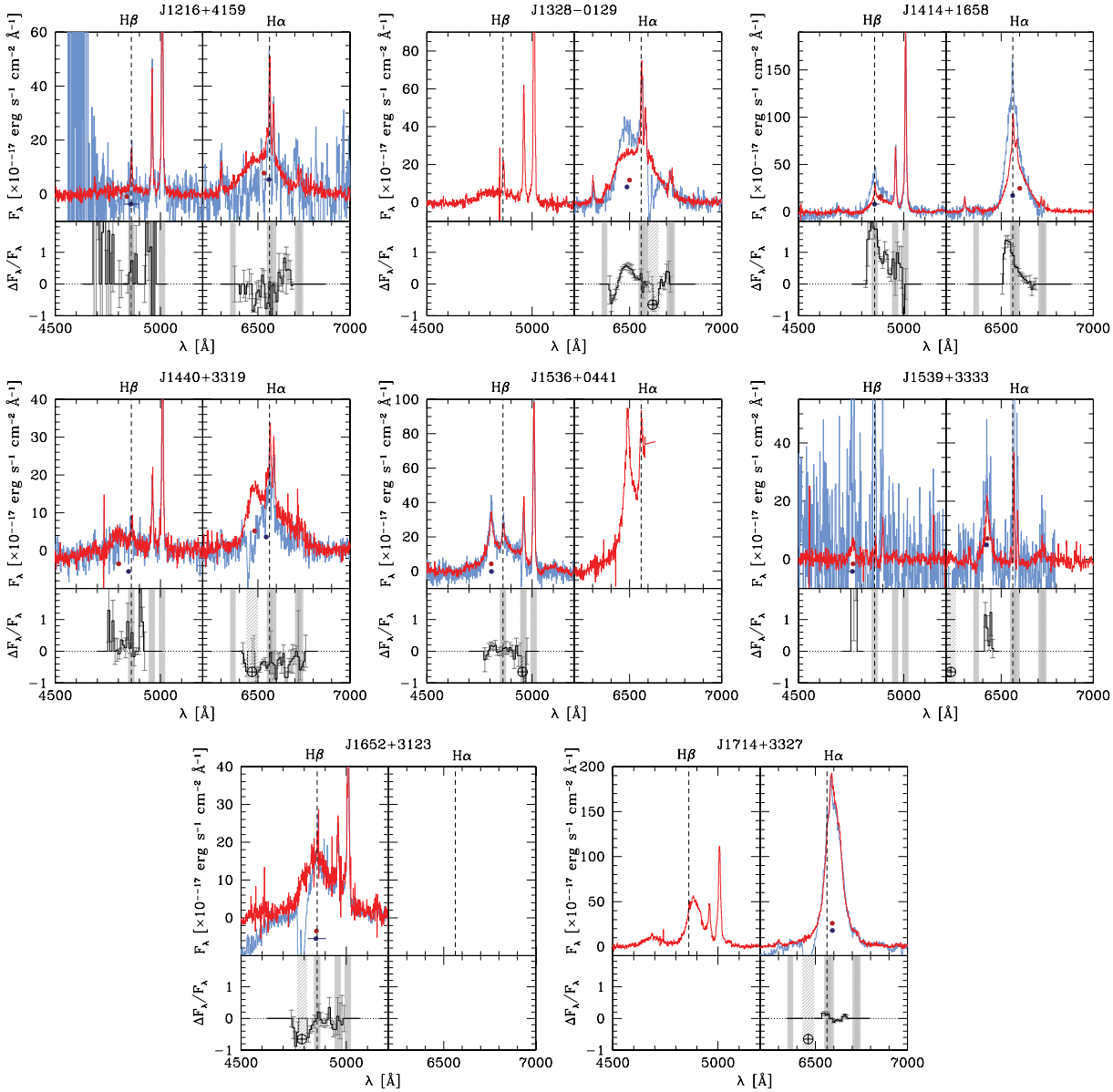

Figure 8. Continuation from Fig. 6.

ACKNOWLEDGEMENTS

We thank Mike Eracleous, Bradley M. Peterson and Brent Groves for useful discussions on the AGN phenomenology. We also thank the Ulli Thiele, Santos Pedraz and the astronomers in Calar Alto for the precious support in the execution of the observations. Support for RD was provided by the DFG priority programme 1573 'The physics of the interstellar medium'. Support for MF was provided by NASA through Hubble Fellowship grant HF-51305.01-A awarded by the Space Telescope Science Institute, which is operated by the Association of Universities for Research in Astronomy, Inc., for NASA, under contract NAS 5-26555. Based on observations collected at the German-Spanish Astronomical Center, Calar Alto, jointly operated by the Max-Planck-Institut für Astronomie Heidelberg and the Instituto de Astrofisica de Andalucia (CSIC). This research has made use of the NASA/IPAC Extragalactic Database (NED) which is operated by the Jet Propulsion Laboratory, California Institute of Technology, under contract with the National Aeronautics and Space Administration. Funding for the Sloan Digital Sky Survey (SDSS) has been provided by the Alfred P. Sloan Foundation, the Participating Institutions, the National Aeronautics and Space Administration, the National Science Foundation, the US Department of Energy, the Japanese Monbukagakusho and the Max Planck Society. The SDSS website is http://www.sdss.org/. The SDSS is managed by the Astrophysical Research Consortium (ARC) for the Participating Institutions. The Participating Institutions are the University of Chicago, Fermilab, the Institute for Advanced Study, the Japan Participation Group, the Johns Hopkins University, the Korean Scientist Group, Los Alamos National Laboratory, the Max-Planck-Institute for Astronomy (MPIA), the Max-Planck-Institute for Astrophysics (MPA), New Mexico State University, University of Pittsburgh, University of Portsmouth, Princeton University, the United States Naval Observatory and the University of Washington.

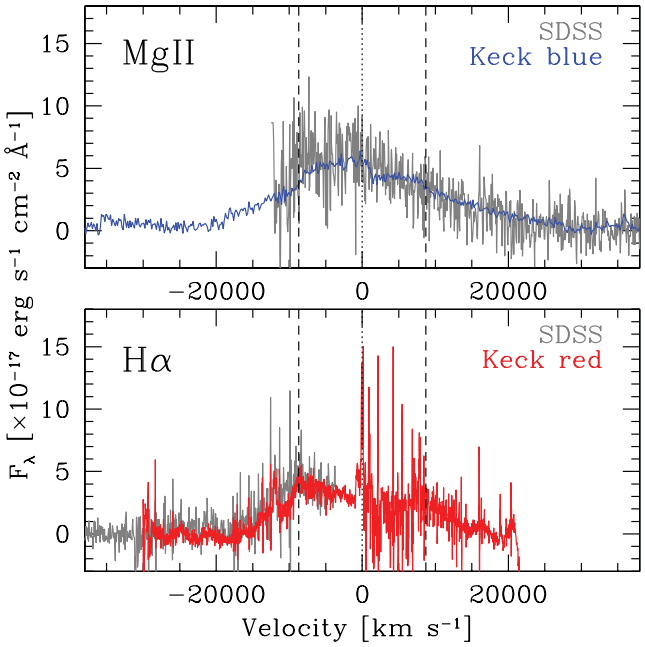

Figure 9. The velocity intervals surrounding Mg II and Hα in J1000+2233. The broad Hβ and Hα lines in the SDSS spectrum peak 8900 km s^{-1} bluewards of the narrow lines (highlighted here with dashed vertical lines; see Decarli et al. 2010b). Our follow-up Keck observations expanded the observed range at both sides of the SDSS data, revealing an 'M'-shaped profile of Hα, and a bell-shaped Mg II line profile, with significantly smaller peak shift. This rules out the BHB hypothesis for this source.

REFERENCES

Ajazajian K. N. et al., 2009, ApJS, 182, 543
Artymowicz P., Lubow S. H., 1994, ApJ, 421, 651
Ballo L., Braito V., Della Ceca R., Maraschi L., Tavecchio F., Dadina M., 2004, ApJ, 600, 634
Barrows R. S., Lacy C. H. S., Kennefick D., Kennefick J., Seigar M. S., 2011, New Astron., 16, 122
Begelman M. C., Blandford R. D., Rees M. J., 1980, Nat, 287, 307
Bentz M. C. et al., 2010, ApJ, 716, 993
Bianchi S., Chiaberge M., Piconcelli E., Guainazzi M., Matt G., 2008, MNRAS, 386, 105
Bogdanovic T., Smith B. D., Sigurdsson S., Eracleous M., 2008, ApJS, 174, 455
Bogdanovic T., Eracleous M., Sigurdsson S., 2009, ApJ, 697, 288
Boroson T. A., Lauer T. R., 2009, Nat, 458, 53
Colpi M., Dotti M., 2009, Adv. Sci. Lett., preprint (arXiv:0906.4339)
De Rosa G., Decarli R., Walter F., Fan X., Jiang L., Kurk J., Pasquali A., Rix H. W., 2011, ApJ, 739, 56
Decarli R., Gavazzi G., Arosio I., Cortese L., Boselli A., Bonfanti C., Colpi M., 2007, MNRAS, 381, 136
Decarli R., Falomo R., Treves A., Kotilainen J. K., Labita M., Scarpa R., 2010a, MNRAS, 402, 2441
Decarli R., Dotti M., Montuori C., Liimets T., Ederoclite A., 2010b, ApJ, 720, L93
Dotti M., Montuori C., Decarli R., Volonteri M., Colpi M., Haardt F., 2009, MNRAS, 398, L73
Dotti M., Sesana A., Decarli R., 2012, Adv. Astron., 2012, E3
Eracleous M., Boroson T. A., Halpern J. P., Liu J., 2012, ApJS, 201, 23
Fabbiano G., Wang J., Elvis M., Risaliti G., 2011, Nat, 477, 431
Gallo E., Treu T., Jacob J., Woo J.-H., Marshall P. J., Antonucci R., 2008, ApJ, 680, 154
Grandi S. A., 1982, ApJ, 255, 25
Groves B. A., Dopita M. A., Sutherland R. S., 2004a, ApJS, 153, 9
Groves B. A., Dopita M. A., Sutherland R. S., 2004b, ApJS, 153, 75
Hayasaki K., Mineshige S., Ho L. C., 2008, ApJ, 682, 1134
Kinney A. L., Calzetti D., Bohlin R. C., McQuade K., Storchi-Bergmann T., Schmitt H. R., 1996, ApJ, 467, 38
Komossa S., Burwitz V., Hasinger G., Predehl P., Kaastra J. S., Ikebe Y., 2003, ApJ, 582, L15
Komossa S., Zhou H., Lu H., 2008, ApJ, 678, L81
Kormendy J., Richstone D., 1995, ARA&A, 33, 581
Koss M. et al., 2011, ApJ, 735, L42
Lauer T. R., Boroson T. A., 2009, ApJ, 703, 930
Lewis K. T., Eracleous M., 2006, ApJ, 642, 711
Maness H. L., Taylor G. B., Zavala R. T., Peck A. B., Pollack L. K., 2004, ApJ, 602, 123
Oke J. B., Cohen J. G., Carr M., Cromer J., Dingizian A., Harris F. H., 1995, PASP, 107, 375
Piconcelli E. et al., 2010, ApJ, 722, L147
Rodriguez C., Taylor G. B., Zavala R. T., Pihlstrom Y. M., Peck A. B., 2006, ApJ, 697, 37
Roedig C., Dotti M., Sesana A., Cuadra J., Colpi M., 2011, MNRAS, 415, 3033
Roedig C., Sesana A., Dotti M., Cuadra J., Amaro-Seoane P., Haardt F., 2012, A&A, 545, 127
Sergeev S. G., Doroshenko V. T., Dzyuba S. A., Peterson B. M., Pogge R. W., Pronik V. I., 2007, ApJ, 668, 708
Sesana A., Roedig C., Reynolds M. T., Dotti M., 2012, MNRAS, 420, 860
Shen Y., Loeb A., 2010, ApJ, 725, 249
Shen Y. et al., 2011, ApJS, 194, 45
Shields G. A. et al., 2009, ApJ, 707, 936
Strateva I. V., Strauss M. A., Hao L., Schlegel D. J., Hall P. B., Gunn J. E., Li L.-X., Ivezić Ž., 2003, AJ, 126, 1720
Tsalmantza P., Hogg D. W., 2012, ApJ, 753, 122
Tsalmantza P., Decarli R., Dotti M., Hogg D. W., 2011, ApJ, 738, 20
Verner E., Bruhweiler F., Johansson S., Peterson B., 2009, Physica Scripta, 134, 014006
Wu X.-B., Liu F. K., 2004, ApJ, 614, 91
York D. G. et al., 2000, AJ, 120, 1579

APPENDIX A: NOTES ON INDIVIDUAL TARGETS

Hereafter we briefly describe the changes observed in sources showing prominent time variability in their line profiles.

J0012−1022: this object shows a dramatic change in the line profile. The knee observed in the red wing of the line in SDSS data disappeared in our follow-up observations (in a rest-frame time lag of ≈8 yr), while the asymmetric blue peak became brighter and shifted bluewards. Such an evolution is not confirmed in the Hβ follow-up observations reported by Eracleous et al. (2012), although the changes may be lost due to the intrinsically fainter line, the confusion with blended Fe II and [O III] emission, and the slightly lower signal-to-noise of their observations.

J0936+5331: the peak of the broad asymmetric line is significantly reduced (but still visible as a knee in the red wing of the lines, roughly at the same wavelength). The drop in the peak flux was already reported by Eracleous et al. (2012), their spectrum dating back to about 1 yr before ours. The brightest part of the line profile is now consistent with the core of the line, closer to $z_{\rm NL}$.

J1117+6741: the profile of broad Hα evolved slightly, producing a shift in the centroid of the line towards shorter wavelengths. This is not clearly observed for Hβ due to the significantly lower line flux.

J1207+0604: the BL peaks are 40 per cent fainter in our second epoch observations, and the blue wings of the line profile are slightly brighter. As a result, the line profile appears boxier, and the line peak shifts bluewards.

J1211+4647: the broad Hβ line became $\sim$10 per cent fainter and shifted slightly redwards, closer to the narrow Hβ line. This source appears also in the sample by Eracleous et al. (2012), but no second epoch spectrum was collected in their follow-up campaign for this source.

J1328−0129: the broad Hα line profile of J1328−0129, as observed in the SDSS data, is boxy and blueshifted of $\approx$3100 km s^{-1} compared with the NLs. Our second epoch spectrum reveals an increase of the flux emission of the blue wing, which now shows a clear peak at $\sim$7470 Å. Note that our conclusions are not affected by the atmospheric absorption feature in the red wing of the line.

J1414+1658: the Balmer lines in this quasar became significantly brighter (by a factor of $\gtrsim$2) and shifted bluewards, closer to $z_{\rm NL}$.

J1440+3319: the broad component of Hα became fainter (by 30–50 per cent). In particular, the asymmetric peak observed in the SDSS spectrum seems disappeared (although our Hα observations are affected by atmospheric absorption at those wavelengths, and the Hβ emission has modest signal-to-noise ratio).

This paper has been typeset from a TEX/LATEX file prepared by the author.